Morphological feature extraction and spectral unmixing of hyperspectral images

Antonio Plaza, Javier Plaza, and Alejandro Cristo
Department of Technology of Computers and Communications, University of Extremadura
Escuela Politecnica de Caceres, Avda. de la Universidad s/n, E-10071 Caceres, SPAIN
E-mail: aplaza@unex.es; Phone: +34 927257195; Fax: +34 927 257203

***Abstract*—Hyperspectral image processing has been a very active area in remote sensing and other application domains in recent years. Despite the availability of a wide range of advanced processing techniques for hyperspectral data analysis, a great majority of available techniques for this purpose are based on the consideration of spectral information separately from spatial information information, and thus the two types of information are not treated simultaneously. In this paper, we describe several innovative spatial/spectral techniques for hyperspectral image processing. The techniques described in this work cover different aspects of hyperspectral image processing such as dimensionality reduction, feature extraction, and spectral unmixing. The techniques addressed in this paper are based on concepts inspired by mathematical morphology, a theory that provides a remarkable framework to achieve the desired integration of spatial and spectral information. The proposed techniques are experimentally validated using standard hyperspectral data sets with ground-truth, and compared to traditional approaches in the hyperspectral imaging literature, revealing that the integration of spatial and spectral information can significantly improve the analysis of hyperspectral scenes when conducted in simultaneous fashion.**

***Index Terms*—Hyperspectral image processing, mathematical morphology, signal processing, spectral unmixing, feature extraction, endmember extraction.**

I. Introduction

Hyperspectral imaging is concerned with the measurement, analysis, and interpretation of spectra acquired from a given scene (or specific object) at a short, medium or long distance by an airborne or satellite sensor [1]. The concept of hyperspectral imaging originated at NASA's Jet Propulsion Laboratory in California, which developed instruments such as the Airborne Imaging Spectrometer (AIS), then called AVIRIS, for Airborne Visible Infra-Red Imaging Spectrometer [2]. This system is now able to cover the wavelength region from 0.4 to 2.5 μm using more than two hundred spectral channels, at nominal spectral resolution of 10 nm. As a result, each pixel vector collected by a hyperspectral instrument can be seen as a *spectral signature* or *fingerprint* of the underlying materials within the pixel (see Fig. 1).

The special characteristics of hyperspectral datasets pose different processing problems, which must be necessarily tackled under specific mathematical formalisms, such as dimensionality reduction or spectral mixture analysis, or data compression [3]. It should be noted, however, that most available hyperspectral data processing techniques have focused on analyzing the data without incorporating information on the spatially adjacent data, i.e., hyperspectral data are usually not treated as images, but as unordered listings of spectral measurements where the spatial coordinates can be randomly

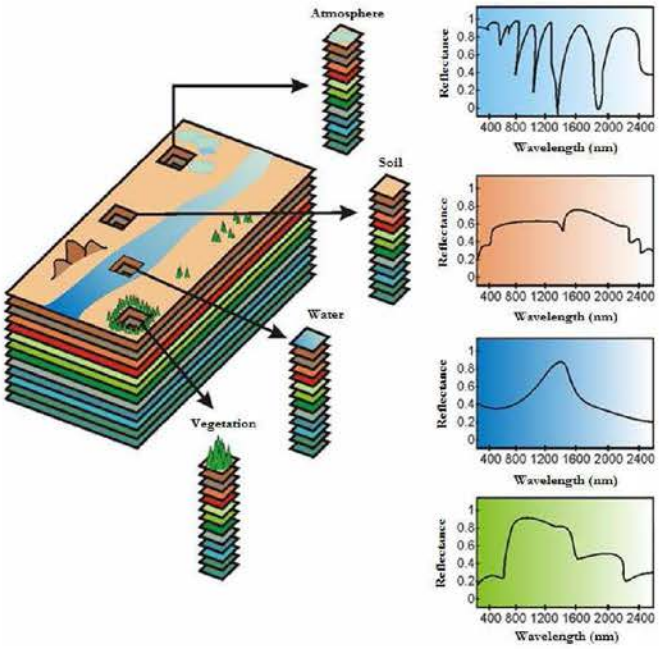

Fig. 1. The concept of hyperspectral imaging.

shuffled without affecting the analysis [4]. However, one of the distinguishing properties of hyperspectral data, as collected by available imaging spectrometers, is the multivariate information coupled with a two-dimensional pictorial representation amenable to image interpretation. Subsequently, there is a need to incorporate the image representation of the data in the development of appropriate application-oriented techniques for the understanding of hyperspectral data [5].

In previous work, we have explored the application of morphological operations to integrate both spatial and spectral responses in hyperspectral data analysis [6]. One of the most widely used dimension reduction techniques in remote sensing is the PCT [3], which computes orthogonal projections that maximize the amount of data variance, and yields a dataset in a new uncorrelated coordinate system. This rotational transform is characterized by its global nature and, therefore, it might not preserve all the information useful to obtain a good classification [7]. In addition, the PCT relies on spectral properties of the data alone, thus neglecting the information related to the spatial arrangement of the pixels in the scene. On the other hand, spectral mixture analysis has been an alluring exploitation goal since the earliest days of hyperspectral imaging [8]. No matter the spatial resolution, in natural environments the

978-1-4244-3555-5/08/$25.00 ©2008 IEEE

spectral signature for a nominal pixel is invariably a mixture of the signatures of the various materials found within the spatial extent of the ground instantaneous field view. In hyperspectral imagery, the number of spectral bands usually exceeds the number of pure spectral components, called endmembers in hyperspectral analysis terminology [9], and the unmixing problem is cast in terms of an over-determined system of equations in which, given the correct set of endmembers allows determination of the actual endmember abundance fractions through a numerical inversion process. Since each observed spectral signal is the result of an actual mixing process, the driving abundances must obey two constraints [10]. First, all abundances must be non-negative. Second, the sum of abundances for a given pixel must be unity. However, it is the derivation and validation of the correct suite of endmembers that has remained a challenging and goal for the past years [11].

In this paper, we develop new morphological techniques for dimensionality reduction and spectral mixture analysis of hyperspectral data sets. The remainder of the paper is structured as follows. Section II presents the proposed framework to extend mathematical morphology to hyperspectral images. Section III develops morphological techniques for dimensionality reduction, endmember extraction and spectral unmixing. Section IV presents experimental results and comparisons to other standardized algorithms in the literature. Finally, Section V concludes with some remarks and hints at plausible future research.

II. Extended mathematical morphology

Mathematical morphology is a theory for spatial structure analysis that was established by introducing fundamental operators applied to two sets [12]. A set is processed by another one having a carefully selected shape and size, known as the structuring element (SE). The two basic operations of mathematical morphology are erosion and dilation. These operators can be graphically illustrated (in the context of greyscale morphology) by viewing the image data as an imaginary topographic relief in which the brighter the gray tone, the higher the corresponding elevation. With this assumption in mind, morphological operations can be interpreted as the result of sliding a SE over the topographical relief, so that the SE defines the new (dilated or eroded) scene based on its spatial properties such as height or width (see Fig. 2).

Extension of morphological operators to multichannel data such as hyperspectral imagery with hundreds of spectral channels is not straightforward. A simple approach consists in applying grayscale morphology techniques to each channel separately, an approach that has been called *marginal morphology* in the literature [13]. However, the marginal approach is often unacceptable in remote sensing applications because, when morphological techniques are applied independently to each image channel, analysis techniques are subject to the well-known problem of *false colors*; that is, it is very likely that new spectral constituents (not present in the original hyperspectral image) may be created as a result of processing

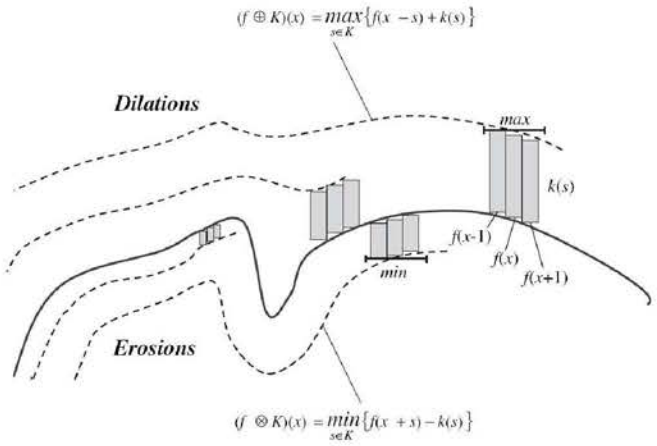

Fig. 2. Graphical interpretation of morphological erosion and dilation operations.

the channels separately. An alternative (and perhaps more appropriate) way to approach the problem of multichannel morphology is to treat the data at each pixel as a vector [14]. Unfortunately, there is no unambiguous means of defining the minimum and maximum values between two vectors of more than one dimension, and thus it is important to define an appropriate arrangement of vectors in the selected vector space.

In this chapter, we develop an application-driven vector ordering technique based on a spectral purity-based criterion [6], where each pixel vector is ordered according to its spectral distance to other neighboring pixel vectors in the N-dimensional data set $\boldsymbol{f}$. More specifically, we adopt a distance-based technique which utilizes a cumulative distance between one particular pixel vector $\boldsymbol{f}(x,y)$, where (x,y) indicates the spatial coordinates, and all the pixel vectors in the spatial neighborhood given by a SE denoted by K as follows [7]:

$$C_K(\boldsymbol{f}(x,y)) = \sum_{(s,t)\in K} \text{SAD}(\boldsymbol{f}(x,y),\boldsymbol{f}(s,t)), \qquad (1)$$

where SAD is the spectral angle distance [10]. The SAD between two pixel vectors $\boldsymbol{f}(x,y)$ and $\boldsymbol{f}(s,t)$ is given by the following expression:

$$\text{SAD}(\boldsymbol{f}(x,y),\boldsymbol{f}(s,t)) = cos^{-1}\left(\frac{\boldsymbol{f}(x,y)\cdot\boldsymbol{f}(s,t)}{\|\boldsymbol{f}(x,y)\|\cdot\|\boldsymbol{f}(s,t)\|}\right). \qquad (2)$$

As a result,$C_K(\boldsymbol{f}(x,y))$ is given by the sum of SAD scores between $\boldsymbol{f}(x,y)$ and every other pixel vector in the K-neighborhood. At this point, we need to be able to define a maximum and an minimum given an arbitrary set of vectors $\mathbf{S} = \{\mathbf{v}_1, \mathbf{v}_2, \cdots, \mathbf{v}_p\}$, where k is the number of vectors in the set. This can be done by computing $C_K(\mathbf{S}) = \{C_K(\mathbf{v}_1), C_K(\mathbf{v}_2), \cdots, C_K(\mathbf{v}_k)\}$ and selecting $\mathbf{v}_i$ such that $C_K(\mathbf{v}_i)$ is the minimum of $C_K(\mathbf{S})$, with $1 \leq i \leq k$. In similar fashion, we can select $\mathbf{v}_j$ such that $C_K(\mathbf{v}_j)$ is the maximum of $C_K(\mathbf{S})$, with $1 \leq j \leq p$. Based on the definitions above, the extended erosion $\boldsymbol{f} \ominus K$ consists of selecting the

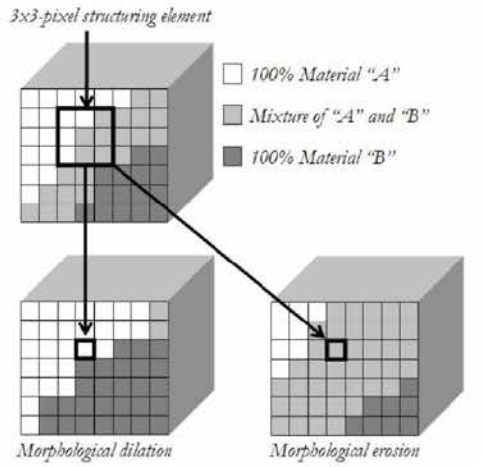

Fig. 3. Toy example illustrating extended morphological operations.

K-neighborhood pixel vector that produces the minimum C_K value as follows [6]:

$$(\boldsymbol{f} \ominus K)(x,y) = argmin_{(s,t)\in K}\{C_K(\boldsymbol{f}(x+s,y+t)\}. \quad (3)$$

On the other hand, the extended dilation $\boldsymbol{f} \oplus K$ selects the K-neighborhood pixel that produces the maximum value for C_K as follows [6]:

$$(\boldsymbol{f} \oplus K)(x,y) = argmax_{(s,t)\in K}\{C_K(\boldsymbol{f}(x-s,y-t)\}. \quad (4)$$

For illustrative purposes, Fig. 3 shows a graphical representation of the performance of these two basic operators using a toy example in which a synthetic hyperspectral image is used for demonstration. As can be seen in Fig. 3, morphological dilation expands the spatial regions made up of pure pixel vectors in accordance with the spatial neighborhood defined by a 3×3 SE, while morphological erosion expands the regions made up of highly mixed pixel vectors in accordance with the same spatial neighborhood. In order to avoid changing the size and shape of the features in the image, a desirable feature for spatial filtering, extended morphological opening and closing operations have also been defined, respectively, as follows: $(\boldsymbol{f} \circ K)(x,y) = [(\boldsymbol{f} \ominus K) \oplus K](x,y)$, i.e., erosion followed by dilation, and $(\boldsymbol{f} \bullet K)(x,y) = [(\boldsymbol{f} \oplus K) \ominus K](x,y)$, i.e., dilation followed by erosion [15].

III. Morphological methods

In the following subsections, we develop novel algorithms for dimensionality reduction via feature extraction, endmember extraction and fractional abundance estimation in hyperspectral images which introduce an innovative component with regards to standard techniques in the literature: the incorporation of spatial information.

A. Morphological dimensionality reduction

In this subsection, we develop a novel algorithm for morphological feature extraction which integrates the spatial and spectral information in simultaneous fashion. To achieve this goal, we apply sequences of extended opening by reconstruction operations using SE's of varying width (called morphological profiles) [15]. This type of morphological sequences have been applied in the past to characterize image structures in grayscale remotely sensed image data [16]. In this subsection, we extend this concept to feature extraction from hyperspectral image data, with the goal to capture the spatial and spectral information around each pixel vector through the combination of spatial-spectral morphological operations for increasingly larger spatial neighborhoods. It is important to emphasize that the use of opening and closing operations is essential for spatial-spectral filtering [7]. With this type of operators, the image features are either completely retained or completely removed in accordance with the size and shape of the structuring element, thus allowing us to perform accurate image filtering based on spatial-spectral content. The inputs to the parallel algorithm, called MORPHDIM, are an N-dimensional hyperspectral image cube, $\boldsymbol{f}$, a maximum number of filtering iterations, t, and a structuring element K with constant size of 3×3 pixels. The output is a transformed image cube, denoted by $\boldsymbol{g}$. The parallel algorithm is given by the following steps:

1) Compute an extended opening by reconstruction for each local pixel $\boldsymbol{f}(x,y)$ as $(\boldsymbol{f} \circ K)^t(x,y) = min_{t\leq1}\{\delta_K^t(\boldsymbol{f} \circ K|\boldsymbol{f})(x,y)\}$, with the basic operation $\delta_K^t(\boldsymbol{f}\circ K|\boldsymbol{f})(x,y) = \delta_B\delta_B\cdots\delta_B(\boldsymbol{f}\circ K|\boldsymbol{f})(x,y)$, i.e., δ_B is applied t times, and $\delta_B(\boldsymbol{f}\circ K|\boldsymbol{f})(x,y) = min\{[(\boldsymbol{f}\circ K)\oplus K](x,y),\boldsymbol{f}(x,y)\}$.
2) Compute an extended closing by reconstruction for each local pixel $\boldsymbol{f}(x,y)$ as $(\boldsymbol{f} \bullet K)^t(x,y) = min_{t\leq1}\{\delta_K^t(\boldsymbol{f} \bullet K|\boldsymbol{f})(x,y)\}$, with the basic operation $\delta_K^t(\boldsymbol{f}\bullet K|\boldsymbol{f})(x,y) = \delta_B\delta_B\cdots\delta_B(\boldsymbol{f}\bullet K|\boldsymbol{f})(x,y)$, i.e., δ_B is applied t times, and $\delta_B(\boldsymbol{f}\bullet K|\boldsymbol{f})(x,y) = min\{[(\boldsymbol{f}\bullet K)\ominus K](x,y),\boldsymbol{f}(x,y)\}$.
3) Compute the derivative of the extended opening profile as follows: $\boldsymbol{p}_t^\circ = \{\text{SAD}[(\boldsymbol{f} \circ K)^\lambda(x,y),(\boldsymbol{f} \circ K)^{\lambda-1}(x,y)]\}$, with $\lambda = \{1,2,\cdots,t\}$. Here, $\boldsymbol{f}(x,y) = (\boldsymbol{f} \circ K)^0(x,y)$ for $\lambda = 0$ by the definition of extended opening by reconstruction.
4) Compute the derivative of the extended closing profile as shown below: $\boldsymbol{p}_t^\bullet = \{\text{SAD}[(\boldsymbol{f} \bullet K)^\lambda(x,y),(\boldsymbol{f} \bullet K)^{\lambda-1}(x,y)]\}$, with $\lambda = \{1,2,\cdots,t\}$. Here, $\boldsymbol{f}(x,y) = (\boldsymbol{f} \bullet K)^0(x,y)$ for $\lambda = 0$ by the definition of extended closing by reconstruction.
5) Form a $(2t-1)$-dimensional morphological profile for each local pixel $\boldsymbol{f}(x,y)$ by combining the derivatives of the extended opening and closing profiles as follows: $\text{MP}(x,y) = \{\boldsymbol{p}_t^\circ(x,y),\boldsymbol{p}_t^\bullet(x,y)\}$. The resulting morphological profile can be seen as a spatial-spectral feature vector for analysis purposes.

B. Morphological endmember extraction

Most available endmember extraction approaches, including popular and successful algorithms such as the PPI (available

in Research Systems ENVI software) [17] or the N-FINDR (distributed by Technical Research Associates, Inc.) [18] have been designed from a spectroscopic viewpoint and, thus, tend to neglect the existing spatial correlation between pixels. In the following, we develop a novel algorithm which integrates the spatial and spectral information in the endmember searching process. The algorithm, based on our previously developed automated morphological endmember extraction (AMEE) algorithm [6], allows propagation of pure pixels between subsequent iterations, as opposed to the previous version of the algorithm. The inputs to the parallel algorithm, called MORPHEE, are the full hyperspectral data cube $\boldsymbol{f}$, a structuring element K, a maximum number of algorithm iterations I_{max}, and a number of endmembers to be extracted, p. The output is an endmember set, $\{\mathbf{e}_i\}_{i=1}^{q}$, with $q \leq p$. A step-by-step description of the algorithm follows:

1) Set $i = 1$ and initialize a morphological eccentricity index [6], denoted by $\text{MEI}(x, y) = 0$, for each pixel $\boldsymbol{f}(x, y)$ in the local partition.
2) Move K through all the pixels of the local partition data, defining a local spatial search area around each pixel $\boldsymbol{f}(x, y)$, and calculate the maximum and minimum pixel vectors at each K-neighborhood using extended morphological erosion and dilation. Then, update the MEI at each spatial location (x, y) using the following expression:

$$\text{MEI}(x, y) = \text{SAD}[(\boldsymbol{f} \ominus K)(x, y), (\boldsymbol{f} \oplus K)(x, y)] \quad (5)$$

3) Set $i = i + 1$. If $i = I_{max}$, then return the MEI scores for all the pixels in the local partition to the master processor. Otherwise, replace the local partition with its dilation using K. This represents an optimization of the algorithm that propagates only the purest pixels at the local neighborhood to the following algorithm iteration. Then, go to step 2.

C. Morphological spectral unmixing

To conclude this section, we outline a new algorithm for fractional abundance estimation of a set of input endmembers. This method integrates the spatial and the spectral information by considering a spatial neighborhood (defined by a morphological SE denoted by K) around each mixed pixel. This method is similar to traditional approaches, in the sense that it makes use of the standard fully constrained least squares technique [10] to estimate abundance fractions. But it differs from traditional methods in the fact that the endmember set used for each pixel is adaptively calculated based on the spatial context. The inputs to the parallel method are the full hyperspectral data cube $\boldsymbol{f}$, a structuring element K, a tolerance threshold t_{SU}, and a set of endmembers $\{\mathbf{e}_i\}_{i=1}^{q}$. The output is an abundance fraction estimation for each endmember in each pixel of the input data set. The algorithm, called MORPHSU, is based on the following steps:

1) Before unmixing a certain local pixel, say $\boldsymbol{f}(x, y)$, a weight is assigned to the pixels in the K-neighborhood centered at spatial coordinates (x, y). This is done by first calculating, for each pixel in the K-neighborhood, the SAD distance to each one of the endmembers in the set $\{\mathbf{e}_i\}_{i=1}^{q}$, and labeling the pixel as an instance of a certain endmember (candidate) by using the minimum SAD score.
2) Then, a weight is assigned to each endmember candidate (the weight is inversely proportional to the minimum SAD score reported for that candidate).
3) Finally, all endmember candidates in the K-neighborhood are sorted by weight, and only those with associated weights above tolerance threshold t_{SU} are incorporated to the *local* endmember set which is finally used to unmix the pixel $\boldsymbol{f}(x, y)$ using standard fully constrained linear spectral unmixing [10]. In other words, the abundance estimation is still performed by using a fully constrained least squares technique [10], but the actual composition of the endmember set used to perform the least squares estimation may vary (for each particular pixel) depending on the spatial-spectral context around the pixel, as opposed to the traditional approach, in which the entire set of spectral endmembers is always used to unmix each pixel. Let us assume that the set of endmembers, obtained by the above procedure, is denoted by $\{\mathbf{e}_i\}_{i=1}^{l}$, with $1 \leq l \leq q$. The goal is to achieve a decomposition of the pixel $\boldsymbol{f}(x, y)$ using the set of l endmembers above as follows:

$$\boldsymbol{f}(x, y) = \mathbf{e}_1 \cdot a_1(x, y) + \mathbf{e}_2 \cdot a_2(x, y) + \cdots + \mathbf{e}_l \cdot a_l(x, y). \quad (6)$$

To achieve this goal, the pixel is multiplied by $(\mathbf{M}^{\mathrm{T}}\mathbf{M})^{-1}\mathbf{M}^{\mathrm{T}}$, where $\mathbf{M} = \{\mathbf{e}_i\}_{i=1}^{l}$ and the superscript 'T' denotes the matrix transpose operation. In the expression above, abundance sum-to-one and non-negativity constraints are imposed, i.e., $\sum_{i=1}^{l} a_i(x, y) = 1$ and $a_i(x, y) \geq 0$ for all (x, y).

IV. Experimental results

This section provides an assessment of the effectiveness of the proposed algorithms in the analysis of a real hyperspectral data set. The image data set used in experiments was collected by NASA Jet Propulsion Laboratory's AVIRIS system over the Cuprite mining district in Nevada was also used in experiments to evaluate the proposed parallel algorithms in the context of a mineral mapping application. The data set (available from http://aviris.jpl.nasa.gov/html/aviris.freedata.html) consists of 614×512 pixels and 224 bands in the wavelength range 0.4–2.5 μm (137 MB in size). It is atmospherically corrected and available in reflectance units (not in at-sensor radiance), thus allowing direct comparison of pixel vectors to ground spectral signatures. The Cuprite site has been extensively mapped by the U.S. Geological Survey (USGS) in the last twenty years, and there is extensive ground-truth information available, including a library of mineral signatures collected on the field (see http://speclab.cr.usgs.gov/spectral-lib.html). Fig. 4(a) shows the spectral band at 587 nm wavelength of

the AVIRIS scene. The spectra of USGS ground minerals: alunite, buddingtonite, calcite, kaolinite, muscovite [Fig. 4(b)], chlorite, jarosite, montmorillonite, nontronite, pyrophilite [Fig. 4(c)] are also displayed. These selected spectral signatures will be used in this work to evaluate endmember extraction accuracy.

We have conducted a cross-validation of spectral unmixing algorithms in the context of a mineral mapping application, using the well-known AVIRIS Cuprite data set in Fig. 4 for demonstration purposes. For comparative purposes, we used the PPI and N-FINDR endmember algorithms to evaluate the performance of the proposed MORPHEE endmember extraction algorithm. Specifically, our experimentation in this subsection comprised the following steps:

1) First, we run PPI and N-FINDR using their original configurations, i.e., using a dimension reduction technique (the PCT in our experiments) to reduce the dimensionality of the input data from N to q (with $q = 15$), obtaining a set of 15 spectral endmembers in both cases. This value was obtained using the VD concept in [19]. In order to establish a fair comparison of our MORPHEE algorithm with the above two algorithms, we also used a reduced version of the original data cube (obtained by the PCT in [20]) when running our algorithm.
2) Then, we repeated the previous experiment but this time using MORPHDIM instead PCT to perform feature extraction from the input hyperspectral scene. Here, we used $t = 8$, resulting in 15 components, which is consistent with the dimensionality estimation provided by the VD concept.

Table I shows the SAD values between the endmembers in the final endmember set (extracted by different combinations of a dimensionality reduction algorithm followed by an endmember extraction algorithm) and the corresponding spectral signatures in the USGS library. In order to display the results in a more effective manner, we only report the SAD score associated to the most similar spectral endmember (out of 15 endmembers obtained for each algorithm combination) with regards to its corresponding USGS signature. It is important to emphasize that smaller SAD values indicate higher spectral similarity. As shown by Table I, the MORPHDIM+MORPHEE combination resulted in the largest number of minimal SAD values (displayed in bold typeface in the table) among all considered combinations. Quite opposite, all the combinations which used MORPHDIM for feature extraction prior to endmember extraction generally produced endmembers which were less similar, spectrally, with regards to reference USGS signatures. This is indeed a very interesting result, which indicates that spatial information can be of great help in the feature extraction task prior to endmember extraction and in the subsequent endmember extraction process. This results from the fact that geological features in the Cuprite mining district exhibit spatial correlation. Therefore, in this example spatial information is important to complement spectral information and discriminate between subtle mineral signatures in this application. As a result, it is not surprising that the performance of PCT in this example was not as good as that exhibited by MORPHDIM, which is particularly tuned for the integration of spatial and spectral information.

We would like to emphasize that the proposed algorithms have also been evaluated from the viewpoint of their capacity to produce high-quality abundance estimations for geological features in the Cuprite mining district. This has been done by estimating the fractional abundance of endmembers provided by PPI, N-FINDR and MORPHEE using the standard linear spectral unmixing (LSU) algorithm and the proposed MORPHSU algorithm for spatial-spectral abundance estimation. In both cases, we tested unconstrained and fully constrained versions (i.e., with sum-to-one and non-negativity restrictions) of the algorithms. Although ground-truth information on endmember fractional abundances at sub-pixel levels is not available for the Cuprite data set (this type of reference information is very difficult to be obtained in real-world scenarios), our quantitative experiments demonstrated that the use of the unconstrained MORPHSU generally resulted in very few negative abundance estimations, while the constrained MORPSHU provided very similar results to those reported by the unconstrained version of the same algorithm. In contrast, a more significant fraction of negative abundances was obtained by the unconstrained LSU with regards to the constrained LSU. It should be noted that a common indicator of poor model fitting and/or inappropriate selection of endmembers is estimation of negative abundance fractions by unconstrained linear models.

Summarizing, experimental results in this section reveal that abundance estimation can be greatly improved by the incorporation of spatial context into the estimation. Standard techniques for fractional abundance determination in the literature have only resorted to the spectral-based techniques, and therefore the use of spatial-spectral information in the unmixing process (after a set of endmembers has been extracted) may greatly assist in the overall estimation.

V. Conclusion

In this work, we have discussed the role of joint spatial-spectral information (via specialized morphological processing) in the analysis of hyperspectral images. Specifically, we have explored the performance of spatial-spectral algorithms for dimensionality reduction, feature extraction, endmember extraction and fractional abundance estimation in the context of a real application domain, i.e., mapping of geological features, using a real hyperspectral data set collected over the Cuprite mining district in Nevada. Our experimental assessment of spatial-spectral algorithms in this application case study revealed important considerations about the properties and nature of such algorithms. The novel spatial-spectral techniques presented in this paper reflect the increasing sophistication of a field that is rapidly maturing at the intersection of many different disciplines, including image and signal processing, sensor design and instrumentation, and environmental modelling. As future work, we plan to implement the full suite

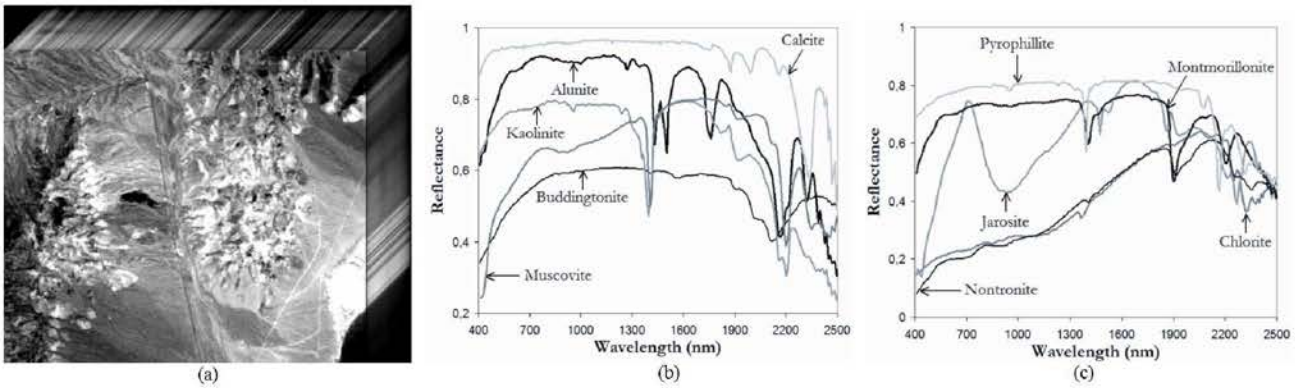

(a) (b) (c)

Fig. 4. (a) AVIRIS scene over Cuprite mining district. (b-c) Ground-truth mineral spectra provided by USGS.

TABLE I

SAD-BASED SPECTRAL SIMILARITY SCORES BETWEEN THE USGS MINERAL SPECTRA AND THEIR CORRESPONDING ENDMEMBER PIXELS PRODUCED BY SEVERAL COMBINATIONS OF A DIMENSIONALITY REDUCTION ALGORITHM FOLLOWED BY AN ENDMEMBER EXTRACTION ALGORITHM.

	Feature extraction using MORPHDIM:			Dimensionality reduction using PCT:		
	PPI	MORPHEE	N-FINDR	PPI	MORPHEE	N-FINDR
Alunite	0.084	0.081	0.084	0.106	0.103	0.095
Buddingtonite	0.106	0.084	0.094	0.122	0.109	0.108
Calcite	0.105	0.105	0.110	0.120	0.112	0.110
Kaolinite	0.125	0.136	0.136	0.144	0.136	0.131
Muscovite	0.136	0.136	0.136	0.153	0.150	0.145
Chlorite	0.112	0.102	0.108	0.135	0.118	0.116
Jarosite	0.106	0.089	0.096	0.122	0.115	0.109
Montmorillonite	0.108	0.094	0.106	0.126	0.119	0.117
Nontronite	0.102	0.099	0.099	0.124	0.120	0.113
Pyrophilite	0.094	0.090	0.090	0.115	0.112	0.105

of spatial-spectral algorithms discussed in this chapter on high performance computing architectures in order to speed up their computational performance. Some of the architectures that are already being used for this purpose include clusters of computers, heterogeneous networks of distributed workstations, field programmable gate arrays (FPGAs) and graphic processing units (GPUs).

REFERENCES

[1] Goetz A F H, Vane G, Solomon J E, Rock B N (1985) Imaging spectrometry for Earth remote sensing. Science, 22:1147–1153

[2] Green R O, et al. (1998) Imaging spectroscopy and the airborne visible/infrared imaging spectrometer (AVIRIS). Remote Sensing of Environment 65:227–248

[3] Richards J A, Xia, J (2006) Remote sensing digital image analysis: an introduction, 4th edition. Springer, Berlin Heidelberg New York

[4] Jimenez L O, Rivera-Medina J L, Rodriguez-Diaz E, Arzuaga-Cruz E, Ramirez-Velez M (2005) Integration of spatial and spectral information by means of unsupervised extraction and classification for homogenous objects applied to multispectral and hyperspectral data. IEEE Trans. Geoscience and Remote Sensing 43:844–851

[5] Gamba P, Dell'Acqua F, Ferrari A, Palmason J A, Benediktsson J A, Arnasson J (2004) Exploiting spectral and spatial information in hyperspectral urban data with high resolution. IEEE Geoscience and Remote Sensing Letters 1:322–326

[6] Plaza A, Martinez P, Perez R, Plaza J (2002) Spatial/spectral endmember extraction by multi-dimensional morphological operations. IEEE Trans. Geoscience and Remote Sensing 40:2025–2041

[7] Plaza A, Martinez P, Plaza J, Perez R (2005) Dimensionality reduction and classification of hyperspectral image data using sequences of extended morphological transformations. IEEE Trans. Geoscience and Remote Sensing 43:466–479

[8] Adams J B, Smith M O, Johnson P E (1986) Spectral mixture modeling: a new analysis of rock and soil types at the Viking Lander 1 site. Journal of Geophysical Research 91:8098–8112

[9] Plaza A, Martinez P, Perez R, Plaza J (2004) A quantitative and comparative analysis of endmember extraction algorithms from hyperspectral data. IEEE Trans. Geoscience and Remote Sensing 42:650–663

[10] Chang C I (2003) Hyperspectral imaging: techniques for spectral detection and classification. Kluwer, New York

[11] Plaza A, Chang C I (2006) Impact of initialization on design of endmember extraction algorithms. IEEE Trans. Geoscience and Remote Sensing 44:3397–3407

[12] Serra J (1982) Image analysis and mathematical morphology. Academic, New York

[13] Comer M, Delp, E (1999) Morphological operations for color image processing. Journal of Electronic Imaging 8:279-289

[14] Soille P (2003) Morphological image analysis: principles and applications. Springer, Berlin Heidelberg New York

[15] Plaza A, Martinez P, Perez R, Plaza J (2004) A new approach to mixed pixel classification of hyperspectral imagery based on extended morphological profiles. Pattern Recognition 37:1097–1116

[16] Benediktsson J A, Palmason J A, Sveinsson, J R (2005) Classification of hyperspectral data from urban areas based on extended morphological profiles. IEEE Trans. Geoscience and Remote Sensing 42:480–491

[17] Boardman J (1993) Automating spectral unmixing of aviris data using convex geometry concepts. In: Green R O (ed) Summaries of Airborne Earth Science Workshop, 111–114. JPL Publication 93-26, Pasadena, CA

[18] Winter M (1999) Algorithm for fast autonomous spectral endmember determination in hyperspectral data. In: Descour M R, Shen S S (eds) Imaging Spectrometry V, 266–275. Proceedings of SPIE

[19] Du Q, Chang C I (2004) Estimation of number of spectrally distinct signal sources in hyperspectral imagery. IEEE Trans. Geoscience and Remote Sensing 42:608–619

[20] Achalakul T, Taylor S (2003) A distributed spectral-screening PCT algorithm. Journal of Parallel and Distributed Computing 63:373-384